Materials Characterization 221 (2025) 114730

Contents lists available at ScienceDirect

Materials Characterization

journal homepage: www.elsevier.com/locate/matchar

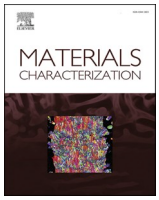

Ni loss and phase structure formed during pulse laser powder bed fusion of Nitinol

Erika Maria Sequeda Leon [a], Teresa Guraya [b], Xabier Lasheras [c], Ana Okariz [b], Karl Peter Davidson [d,e], Sarat Singamneni [a], Zhan Wen Chen [a,*]

[a] Department of Mechanical Engineering, Auckland University of Technology, Auckland, New Zealand
[b] Department of Mining & Metallurgical Engineering & Materials Science, University of the Basque Country UPV/EHU, Bilbao, Spain
[c] Azterlan, Basque Research and Technology Alliance (BRTA), Durango, Spain
[d] School of Materials Science and Engineering, Nanyang Technological University, Singapore
[e] Photon Forge Additive Manufacturing Facility, John de Laeter Centre (JdLC), Curtin University, Perth, Australia

ARTICLE INFO

Keywords:
Ni content
Parameters
Defects
Austenite
Martensite

ABSTRACT

In recent years, there has been a significant research effort in the laser powder bed fusion (LPBF) processing of Nitinol aiming potentially for stenting applications. To achieve superelasticity that Nitinol stents require, Ni content needs to be within ±0.1at% of the optimal Ni content of 50.8at%, but the high thermal intensity of the laser in LPBF results in a Ni-loss. How to achieve the targeted Ni content in LPBF processed Nitinol alloys, whilst producing defect-free parts is not certain, requiring further evaluation. In the LPBF processing of a Nitinol powder with 51.2at% Ni herein, we exhibit defect-free processing obtaining the idealised Ni content with the use of a constant scan velocity and narrow power and thus energy (E) window. An exponential decay in Ni content with increasing E was observed and is correlated to the aspect ratio of the melt pool shape. Under optimum, defect free conditions, a primarily austenite structure with a tiny amount of twinned martensite is reported by room temperature. Sequential transmission electron micrographs taken between −80 °C to 0 °C on a defect-free sample have illustrated the transformation of twinned martensite to austenite with the major portion of the transformation taking place well below 0 °C.

1. Introduction

Laser powder bed fusion (LPBF) has matured to become an important manufacturing technology and is more widely adopted by industry after intensive research in process optimisation and microstructure control of parts since the early-mid 2000s [1,2]. The most distinctive advantage of LPBF is its capability of producing parts with minimal geometrical restrictions and with a feature thickness as small as ~0.1 mm [3], and is ideal for customised and low-volume production [4]. These capabilities have also driven the study in the processability of Nitinol (an equiatomic or near equiatomic NiTi alloy) during the 2010s, with the alloy widely applied in the manufacture of biomedical devices, complex to make using traditional manufacturing processes [5–13]. In these seminal studies, the focus was on establishing a processing window of the alloy to create parts free of lack-of-fusion defects and keyhole pores.

The dominant use of Nitinol in biomedical applications is in the manufacture of stents. The functional property that a Nitinol stenting alloy can provide is the excellent superelasticity at temperatures between room (~22 °C) and body temperature (37 °C). In Nitinol's austenitic state, under loading at a determined critical stress (σ_c) level, the transformation of austenite→martensite (A → M or B2 → B19) occurs with a subsequent ~6 % strain increase. Relieving the applied stress results in M → A thus, releasing this strain. This transformation induced strain is referred to as pseudoelasticity (or superelasticity). Nitinol can also be in a twinned martensitic (B19') state at low temperatures. Taking this into consideration, in the stenting application, the temperature (A_f) at which (twinned) M → A transformation is fulfilled should be close to 22 °C. However, A_f should also be close to 37 °C, as the critical stress for A → M is lower at higher A_f temperatures [14].

To meet the requirements of A_f and σ_c in the application of stents, the industry standard Nitinol alloy consists of 50.8at% Ni [15], determined from the extensive tests conducted during 1990s–2000s [16–19]. In an extensive series of experiments using Ni contents between 44.0 and 51.2at.%, Frenzel et al. [20] reported that A_f is basically unchanged at

* Corresponding author.
E-mail address: zhan.chen@aut.ac.nz (Z.W. Chen).

https://doi.org/10.1016/j.matchar.2025.114730
Received 29 October 2024; Received in revised form 14 December 2024; Accepted 8 January 2025
Available online 10 January 2025

Table 1
Analytical methods of powder ($Analy_P$), Ni content of powder (at.%Ni_P), analytical methods of samples ($Analy_S$), Ni content of samples (at.%Ni_S), change of Ni content (Δat.%Ni) in various studies.

$Analy_P$	At% Ni_P	$Analy_S$	E and at%Ni_S	Δat%Ni	Ref.
SEM-EDS	50.01	SEM-EDS	22-100 J/mm^3, 49.98 to 45.93, not related to E	−0.03 to −4.08	[29]
ICP-AES	50.32	ICP-AES	40-260 J/mm^3, one 50.32 & other six 50.22	0 to −0.1	[30]
ICP-AES	50.63	ICP-AES	45-125 J/mm^3, 50.58 to 49.82 linear, high scatters	−0.05 to −0.81	[31]
SEM-EDS	50.1 ± 0.9	SEM-EDS	86 & 118 W, 50.2 ± 0.6 & 50.2 ± 0.5, respectively	+0.1	[32]
EDS & ICP?	49.96	EDS & ICP?	47-99 J/mm^3, 49.80 to 49.68	−0.16 to −0.28	[33]
SEM-EDS	50.01	SEM-EDS	12 E values, between 50.21 and 49.75, trend no clear	0.20 to −0.26	[34]
SEM-EDS	50.9	SEM-EDS	1.2–0.4 m/s, 50.7 to 50.3	−0.2 to −0.6	[35]
ICP?	50.02	ICP	6 E values, 50.40, 50.46, 50.51, 50.93, 50.75, 51.09	1.07 to 0.39	[36]
ICP-AES	50.91	SEM-EDS	41-67 J/mm^3, 50.58	−0.23	[37]
ICP-AES	50.91	SEM-EDS	Six E conditions, from 50.28 to 49.70, large scatters	−0.62 to −1.21	[38]

~108 °C for Ni ≤ 50at.%. At Ni > 50.0at%, the A_f decreases sharply as at %Ni increases following the relationship: $d(A_f)/d(Ni) \approx -8.5$ °C/0.1at %. Thus, for $A_f = 37$ °C, the Ni concentration is 50.8at%, explaining the Ni content value widely used for Nitinol stenting purposes. For the same reason, this is the widely reported composition in the processing of Nitinol by LPBF [21–28]. However, the high energy beam in LPBF can results in composition variance with Ni loss occurring as the vaporisation temperature of Ni (2730 °C) is significantly lower than that of Ti (3287 °C). In the numerous reviews on Nitinol processed by LPBF [5–13], the loss in Ni content is well reported [7–9,11]. It has also been suggested that tuning of LPBF parameters may enable an optimum A_f to be achieved [11]. However, the compositional difference after LPBF and custom compositions tailoring Ni content to achieve 50.8at% after LPBF processing have not been realised.

In order to understand how the LPBF process changes the Ni content in Nitinol through vaporisation, a summary of difference in Ni content for Nitinol alloys before and after LPBF from various studies is presented in Table 1. In these studies, various laser energy (E), in J/mm^3, values were used as defined by:

$$E = \frac{P}{v \times h \times t} \quad \text{(n. 1)}$$

where P (J) is the laser power, v is the scanning rate (mm/s) h is the hatch spacing (mm) and t layer thickness (mm) [4]. A wide range in Ni loss was reported by Obeidi et al. [29] up to ~4at%, as detected using scanning electron microscope coupled with energy-dispersive X-ray spectroscopy (SEM-EDS) capability. In this study, the loss has not been found to depend on E. Applying inductively coupled plasma (ICP) spectroscopy analysis, Chen et al. [30] showed little loss of Ni over a wide range of E values, whilst Safdel et al. [31] determined the loss up to 0.81at%, being linearly dependent on the E value although error is high. Both Zhu et al. [33] and Obeidi [34], through the use of SEM/EDS, reported a slight Ni loss (≤0.2at%) at low E to 0.3at% at high E. Yet Guo et al. [35] reported Ni loss from 0.2 to 0.6at% with increasing E values. The use of repetitive laser scanning was reported by Zhan et al. [37,38] to result in a high Ni loss, contributing to their low σ_c values (122-169 MPa), expected as with Ni < <50.8at%, a high portion of the structure should be martensitic. There is an overarching trend in the loss of Ni when processed by LPBF, however, Maffia et al. [32] and Shen et al. reported a gain in Ni content after LPBF by both SEM-EDS and ICP chemical analysis methods [36].

Table 2
Laser power and energy values used in the LPBF experiments.

P (W)	63	81	100	119	138	156	175	194
E, (J/mm^3)	34	44	55	65	75	85	96	106

As evident from the literature data, there is a lack of clarity on the Ni loss during LPBF of Nitinol, particularly in the amount of Ni loss and, how the composition fluctuates with laser energy (E). Furthermore, the relationship between laser energy, Ni loss and the formation of lack of fusion (LOF) or keyhole pores has not been evaluated. Thus, herein this study aims to systematically evaluate how E influences the Ni content of the alloy. This is achieved by varying P while keeping v (also the pulsing parameters) the same. X-ray diffraction (XRD) analysis has been conducted to reveal the phases present in the as-built samples that have experienced the different amount of Ni loss. The present investigation has also aimed at identifying the window of conditions that, while LPBF may result in suitable Ni content in the as-print samples using the suitable LPBF conditions, the conditions can also be for defect-free printing. Finally, using a selected sample, observation on phase transformation has been made using transmission electron microscopy (TEM) to illustrate how M → A over a temperature range for a better understanding on the transformation behaviour.

2. Experimental procedures

The as-received powder (15-53 μm in size, from Hermus & OEM) was first chemically analysed for its Ni content. Powder particles were dissolved in an aqua regia-hydrofluoric acid mixture and then the analysis was carried out using a Thermo Fisher Scientific iCAP 7400 inductively coupled plasma optical emission spectroscope (ICP-OES). The analysis has shown a Ni content of 51.2at.%. A Renishaw AM400 LPBF system was used to make samples, equipped with a 400 W ytterbium fibre laser operating in a pulsed laser mode with a wavelength of 1.070 μm. In this work, a reduced-size attachment was used so that LPBF experiments could be conducted with a reduced amount of powder. For all the LPBF experiments, hatch spacing (h) and layer thickness (t) were constant at 64 and 40 μm respectively. The pulse laser conditions consisted of a point distance (d_p) of 50 μm and, a laser on and off time within a pulse cycle of 60 and 10 μs respectively. The laser power (P) was varied as presented in Table 2, resulting in the corresponding laser energy (E) values:

$$E = \frac{P \times (t_{on} + t_{off})}{d_p \times h \times t} \quad \text{(n. 2)}$$

After LPBF processing, samples were cut off the build platform and sectioned parallel to the build direction (BD), followed by conventional metallographic preparation techniques; mounting, grinding and polishing. These samples were then used for defect analysis, microstructure observation, XRD and TEM observation. To observe microstructures, polished samples were etched with Kroll's reagent: 87.7 % H_2O, 14.1 % HNO_3, and 3.2 %HF for 30 s. Microstructures were examined by optical microscopy and by a Hitachi SU-70 scanning electron microscope (SEM) with energy-dispersive X-ray spectroscopy (EDS) capability. The fraction of LOF (f_{LOF}) and keyhole porosity (f_{Pores}) were measured form images taken of the polished surface prior to etching. For each sample, 12 images were taken and ImageJ imaging software was used to determine the f_{LOF} and f_{Pores}. For measuring LOF in each image using the software, the spherical (and partially spherical) keyhole pores were manually removed. For measuring keyhole pores, the non-spherical LOF pores were manually removed. Electron backscatter diffraction (EBSD) mapping was conducted on the sample produced with the most promising parameters (E = 55 J/mm^3). For this, a JEOL JSM-7000F SEM

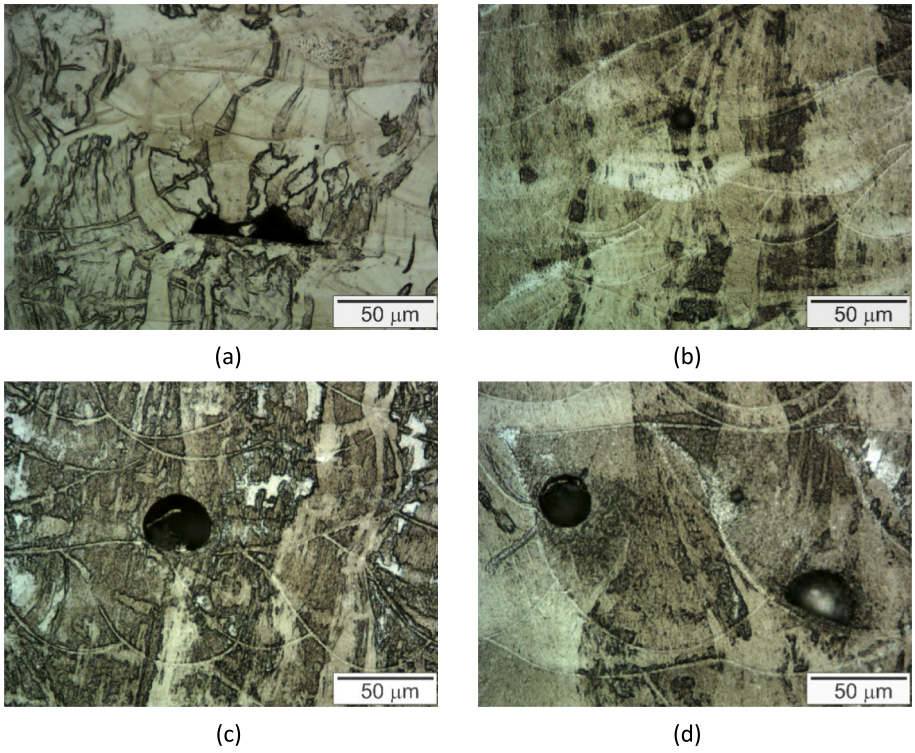

Fig. 1. Optical micrographs of LPBF samples made using laser energy density (E): (a) 44 J/mm^3 displaying a LOF defect, (b) 65 J/mm^3 and (c) 85 J/mm^3 displaying a keyhole pore, and (d) 106 J/mm^3 displaying two keyhole pores.

equipped with EBSD (Oxford CMOS) capability was used.

The composition and Ni concentration of virgin powder and LPBF samples was measured by EDS. As this is not a fully quantitative analysis technique, EDS measurements of Ni content were corrected against the virgin Nitinol powder through the use ICP-OES. The difference in Ni content between ICP-OES and SEM/EDS methods was used in the correction of Ni content of LPBF built samples detected by SEM/EDS. XRD patterns were collected by a PHILIPS X'PERT PRO automatic diffractometer operating at 40 kV and 40 mA, in θ-θ configuration with a secondary monochromator with Cu-Kα radiation (λ = 1.5418 Å) and a PIXcel solid state detector (active length in 2θ 3.347°). A 2θ range of 10–80° was evaluated, at a step size of 0.026° and a scan speed of 0.011°/s. Diffraction experiments were conducted at room temperature with a 1° fixed soller and divergence slits giving a constant volume of sample illumination.

To observe M → A transformation a TEM specimen (50-60 nm thick lamella) was taken from the sample produced at a E of 55 J/mm^3. A standard lift out protocol was employed using an Omniprobe micro-manipulator mounted on a focused ion beam Helios NanoLab 650 dual beam system. TEM room temperature imaging was conducted on an image-corrected Thermo Fisher Titan Cube 60–300 microscope and low temperature imaging (<0 °C) was carried out on a Tecnai F30 microscope (FEI Company). TEM images were obtained with a coupled CCD camera (Gatan). Low temperature was achieved using a cryoholder, with the ability to cool the sample to −170 °C using liquid N_2. Once the temperature stabilised and the sample was able to be fully transformed into martensite, the sample was heated to −40 °C at a rate of 10 °C/min, followed by heating to 0 °C at a rate of 3 °C/min. A series of Images were recorded during the heating period and were subsequently processed with the software TIA from FEI.

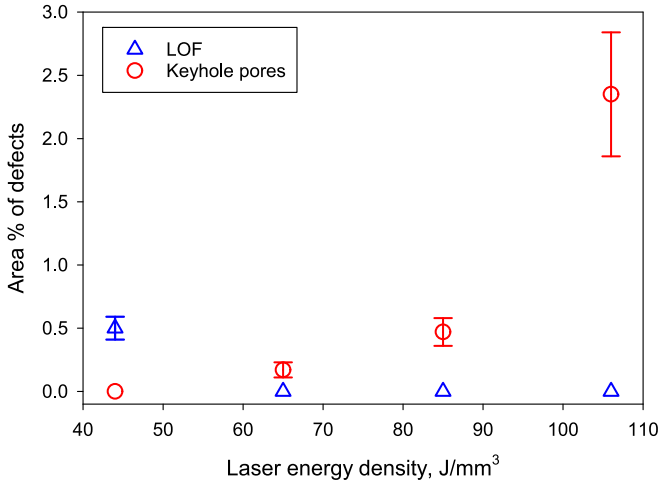

Fig. 2. Area fractions (mean and standard error values) of LOF and keyhole pores in LPBF samples made using laser energy density (E) of 44, 65, 85 and 106 J/mm^3.

3. Results and discussion

3.1. Defect levels and laser powder/energy

Representative cross-sectional optical micrographs of LPBF samples made using E = 44, 65, 85 and 106 J/mm^3 are shown in Fig. 1. The formation of LOF defects was observed in the samples produced at the lowest E of 44 J/mm^3 (Fig. 1a). This type of defect disappears in higher E value samples, simply as a result of the higher E and thus larger molten and solidified tracks fully overlapping to prevent LOF. The relationship between laser powder (and thus E while other parameters are kept unchanged) and the amount of LOF has long been well studied and been

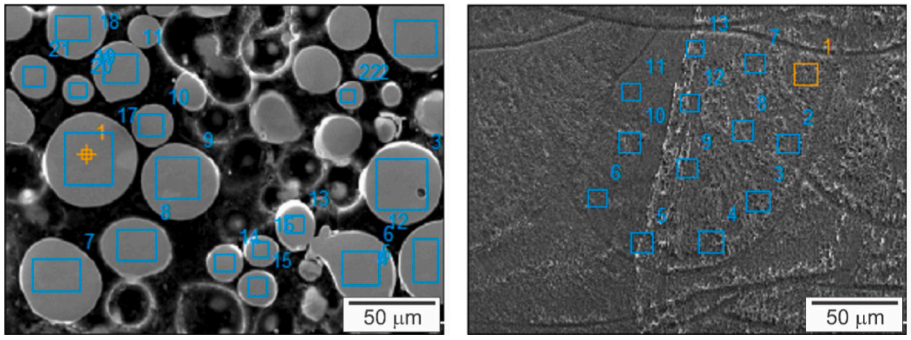

Fig. 3. SEM images of Nitinol (a) powder and (b) LPBF produced sample, with blue squares representing SEM-EDS measurement locations.

Table 3
Ni content of powder and LPBF samples with respect to laser energy density, loss in Ni content (ΔNi) after LPBF and change in Ni content loss over change in laser energy density represented as ΔΔNi/ΔE. Notes: Non-corrected measurements were determined by SEM-EDS (including standard error values based on $n = 10$) and corrected values were based on using the ICP analysis of powder.

	Powder	34 J/mm^3	44 J/mm^3	55 J/mm^3	65 J/mm^3	75 J/mm^3	85 J/mm^3	96 J/mm^3	106 J/mm^3
Non-corrected (at.%)	50.68	50.54	50.37	50.26	50.19	50.12	50.07	50.09	50.06
	±0.06	±0.02	±0.03	±0.04	±0.04	±0.05	±0.05	±0.04	±0.02
Corrected (at%)	51.20	51.06	50.89	50.78	50.71	50.64	50.59	50.61	50.58
ΔNi(at%)		−0.14	−0.31	−0.42	−0.49	−0.56	−0.61	−0.59	−0.62
ΔΔNi/ΔE (at%/Jmm^{-3})			−0.017	−0.010	−0.007	−0.007	−0.003	0.002	−0.003

well reviewed [1]. The studies to understand how process parameters affecting the size and shape of the melt pool which affect the degree of overlapping and in turn the amount of LOF during LPBF has continued [4,39].

However, at elevated E values, keyhole pores are present, as seen in Fig. 1b to Fig. 1d, attributed to the formation of deep keyhole melt pools by virtue of the narrow-focussed energy source in which vapour is trapped in the melt pool leading to their formation. This phenomenon has also been well studied [1,4]. At intermediate E values, (Fig. 1b), LOF is mitigated and keyhole formation can occur. Area fractions of LOF (f_{LOF}) and keyhole pores (f_{Pores}) were taken from optical images of the four samples (E = 44, 65, 85 and 106 J/mm^3) and the calculated values are plotted against E in Fig. 2. As is evident in Fig. 1b, keyhole pores are present in the sample produced at E = 65 J/mm^3 suggesting an onset of keyhole melt mode at this E. Although no data are plotted for sample 55 J/mm^3 in the figure, both LOF and porosity defects are not present in the sample. Thus, as suggested in Fig. 2, defects-free LPBF can be achieved using E = (55–60)J/mm^3.

3.2. Composition change with laser energy

Both the powder and built samples were analysed using SEM/EDS and examples of such measurements are shown in Fig. 3. Multiple measurements were recorded to obtain statistical accuracy and all Ni contents, corrected and non-corrected are listed in Table 3. The standard error values are determined to be <0.1at.% and thus there is a high certainty in the mean values reported. Overall, it is evident that the thermally intensive LPBF process resulted in a loss of Ni content, with this loss E dependant. At the lowest E, 34 J/mm^3, the loss (ΔNi) is minimal (0.14at.%). However, as E increases within the low-medium range (44-65 J/mm^3), ΔNi increases but the rate (ΔΔNi/ΔE) decreases. At the high E range (85-106 J/mm^3) the values of ΔΔNi/ΔE are very low. The measurements taken from SEM-EDS analysis, without the use of a standard sample is semi-quantitative, but the difference (ΔNi) between each sample can be viewed to be reliable, as is ΔNi as a function of E presented in Table 3.

Quantitative composition analysis was established via ICP-MS, with

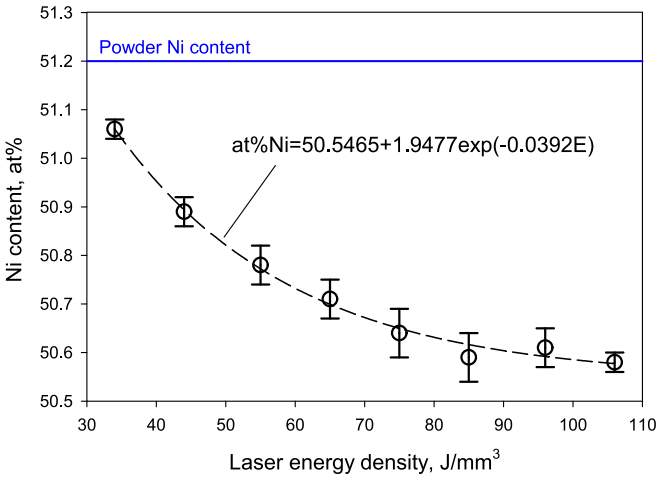

Fig. 4. Corrected Ni content (mean and standard error) of LPBF samples plotted as a function of laser energy density, together with the initial Ni content in powder and a fitted exponential decay curve.

the powder Ni content measured to be 51.2at%, yielding a difference of 0.52at.% when compared to SEM-EDS (Ni = 50.68at.%). Knowing this, by adding this difference (0.52at.%) to those measured via SEM-EDS, the Ni content can be viewed as corrected, without affecting ΔNi and ΔΔNi/ΔE. These corrected Ni content values are plotted against E in Fig. 4, together with a fitted curve with an exponential decay function. As observed in the curve of Fig. 4, at the low E range (from E = 34 J/mm^3), ΔNi is low but ΔΔNi/ΔE is high, indicative of a rapid decay in Ni content with increasing E. Further increase in E results in the decrease in ΔΔNi/ΔE. This trend in the data and fitted curve of decay is reasonable if the LPBF melt pool volume as a function of E is considered. Given a constant laser beam size (~70 µm) for all E values and given that E was adjusted by changing P whilst keeping all other parameters constant, the increase in melt volume should be dominantly the result of increasing the depth of the melt pool rather than the width. Ni loss by vaperisation shoud

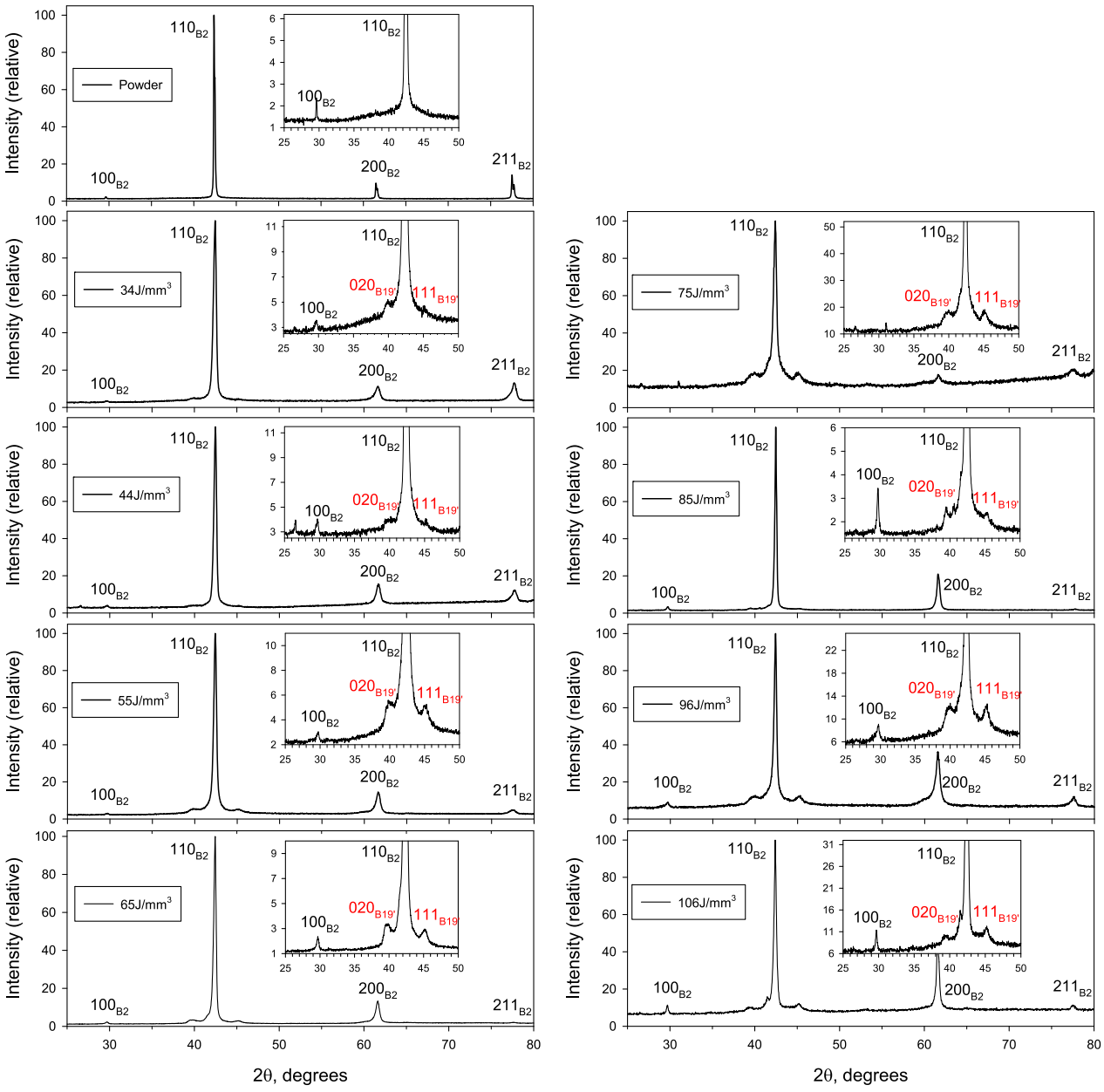

Fig. 5. X-ray diffraction patterns (relative intensity vs. 2θ) of powder and LPBF samples made using E from 34 to 106 J/mm^3 showing pure B2 phase in the powder sample and generally weak but stronger peaks of diffractions from B19' in LPBF samples as E increases.

depends on the area of the melt surface. Thus, the restricted increase in the witdh of the melt as E increases should also prevent ΔΔNi/ΔE to be high.

As we have explained (in Introduction), the amount of Ni loss and how the Ni content changes with the change of laser energy (E) have not been clear. Our aim is to identify the amount of Ni loss (decrease in at.% Ni) as a function of laser power (thus laser energy) while keeping other parameters the same and, as shown in Fig. 4, the loss has been identified to follow an exponential decay trend. Therefore, adjusting laser power level and thus energy to reach 50.8at.%Ni after LPBF is possible. It is also important and thus our aim to know the energy level for the minimum level of LOF and keyhole pores, keeping in mind the requirement of Ni content in the as-built samples/parts. This has also been demonstrated in Fig. 2. The further important requirement is the structure after LPBF and the analysis of the as-built samples is presented below.

3.3. Structure change with increasing Ni loss

The response of phase constituent formation induced by the loss of Ni after LPBF processing can be understood through the analysis of XRD patterns as shown in Fig. 5. For each sample, a full scan XRD pattern (2θ = 25–80°) is plotted covering the major diffraction peaks for the phases present in the samples. In addition, for each pattern, an inset highlighting the 2θ from 25 to 50° with the intensity scaled up many times but keeping the background noise similar for all inset patterns. Thus, the small diffraction peaks are clearer and these small peaks in one inset pattern graph can be compared to other inset pattern graphs. As will be shown and explained, this is necessary as the diffraction peaks from B19's are small.

In the powder sample (top-left in Fig. 5), there are three major diffraction peaks, at 2θ ≈ 42.5°, 61.6° and 77.7°. In accordance to JCPDS 18–899 [40], for the B2 NiTi (a = 0.2998 nm) and using λ = 0.154 nm, the first three diffractions; 110, 200 and 211 correspond to diffraction

Table 4
Normalised (to 100) intensity of 110, 200, and 211 diffractions of B2 in various samples.

Sample	I_{100}	I_{110}	I_{200}	I_{211}
Powder	1.1	100	8	13
34 J/mm^3	0.8	100	8	10
44 J/mm^3	1.2	100	10	6
55 J/mm^3	0.8	100	12	2
65 J/mm^3	1.2	100	12	1
75 J/mm^3	Uncertain & <0.3	100	6	4
85 J/mm^3	1.8	100	23	1
96 J/mm^3	3.5	100	32	7
106 J/mm^3	5.4	100	40	2

peaks at 42.59°, 61.81° and 77.96°, respectively. The measured 2θ values are very close to the reference JCPDS card (42.5° compared to 42.59°, 61.6° to 61.81°, and 77.7° to 77.96°) for the peaks of the powder sample, confirming the 110, 200 and 211 diffractions. Thus, the powder consists solely of the B2 structure, irrespective of difference in the normalised intensity (I/I_o) values compared to the JCPDS card.

As shown in the pattern for the powder (and also other samples) in the insets of Fig. 5, there is an additional small peak at 2θ ≈ 29.7°, corresponding to 100 diffraction. In the diffraction in a single element BCC structure, h + k + l should be even. But as Nitinol is a near-equiatomic Ni—Ti alloy, simulations have suggested 100 diffraction occurs with a peak of a small to medium intensity [41]. Examining all patterns in Fig. 5, 100 diffraction is present in each LPBF sample, except at 75 J/mm^3 for which the 100 peak is inconclusive. Additionally, the 200 peak in the 75 J/mm^3 is comparatively the weakest, as summarised in Table 4. This is expected as (200) and (100} are parallel and thus a stronger 200 peak should generally result in a stronger 100 peak. It may be noted that the intensity of 110_{B2} in the 75 J/mm^3 sample is not weak. Grain growth during LPBF normally results in the {100} preferred orientation along the build direction in cubic alloys. As the LPBF sample surface for XRD is parallel to the build direction, there is not a preferred orientation and strong 100 and 200 diffractions are not observed. However, it is uncertain as to why 200 and thus 100 diffractions become relatively stronger in high E (85-106 J/mm^3) value samples, after having relatively the weakest 200 peak for at 75 J/mm^3, as seen in Table 4.

In the XRD patterns for the LPBF samples, shown in Fig. 5, small diffraction peaks are evident near the 110_{B2} peak, as observed in the inset graphs. Take for example the pattern for the 55 J/mm^3 sample, the peak to the left and right side of the 110_{B2} peak are at 2θ values of 39.5° and 45.1° respectively. According to JCPDS file 35–1281 [40], these peaks can be identified as diffractions from (020) and/or $(1\bar{1}1)$ of B19's for the first and (111) of B19' for the second. The 020 diffraction at 39.22° is the third most intensive diffraction, $1\bar{1}1$ at 41.36° the strongest, 111 at 44.93° the second strongest according to the file. Thus, the presence of B19' in the 55 J/mm^3 sample is validated. The amount of B19' is however not certain as comparing I values is not reliable due to the sample not being in a powder form. It may be suggested that the amount of B19' is very small, with the relative intensity of the strongest peak from $111_{B19'}$ being only slightly over 1 % of that for 110_{B2}.

At the lower E (34 and 44 J/mm^3) values, the presence of B19' may still be certain, identified in the XRD zoom-in (inset) patterns in Fig. 5, although the B19' diffraction peaks are significantly weaker than those seen in the pattern of 55 J/mm^3 sample. Numerically, $I_{111B19'}/I_{110B2}$ for samples 34 and 44 J/mm^3 are both estimated to be less than 1 %, compared to slightly over 1 % for sample 55 J/mm^3. On the left side of the 110_{B2} peak in the pattern of sample 44 J/mm^3, there is not a sharp peak but a small flat top. As has already been explained, 020 at 39.22° and $1\bar{1}1$ at 2θ = 41.36° are strong peaks for B19' according the JCPDS file and there could be contributions from both. Furthermore, the small peaks are very close to the strong peak from 110_{B2}. Thus, a small flat top rather than a sharp peak is not viewed of as unusual.

For the sample built using the next higher E level (> 55 J/mm^3) at 65 J/mm^3, the peaks near the 110_{B2} peak shown in Fig. 5 are clearly evident. It appears that the peak on the left may be contributed more from $020_{B19'}$ diffraction as 2θ is at ~39.1°. For the less ambiguous B19's diffraction $111_{B19'}$, $I_{111B19'}/I_{110B2}$ ≈ 1 %, slightly lower than that the pattern for sample 55 J/mm^3. However, the amount of B19's in a sample cannot purely be based on the $I_{111B19'}/I_{110B2}$ as the samples for XRD are not in powder form. For sample 75 J/mm^3, diffractions from B19' are clear and $I_{111B19'}/I_{110B2}$ has increased to ~4 %. This increase, however, does not apply to the next higher E sample with $I_{111B19'}/I_{110B2}$ having decreased to ~0.5 % although the $111_{B19'}$ peak can be certain. Patterns of higher E (96 and 106 J/mm^3) samples in Fig. 5 show that $I_{111B19'}/I_{110B2}$ is ~4 % for the 96 J/mm^3 samples and ~ 3 % for the 106 J/mm^3 samples, respectively. In the pattern for the 106 J/mm^3 sample, $1\bar{1}1_{B19'}$ deflection at is 2θ = 41.5° is clear.

As per the discussion above, XRD patterns (Fig. 5) highlight the presence of B19' phase in all LPBF samples at room temperature. The ratio of $I_{111B19'}/I_{110B2}$ from XRD of LPBF samples as a function of E cannot be clearly established and intensity comparisons on non-powder samples XRD is not the base for estimating the relatively amount of the phases in the sample. However, the patterns for high E samples may have generally but not consistently shown that these samples contain a slightly higher amount of B19'. The analysis may also have suggested that for the condition of defect-free LPBF at 55-60 J/mm^3, with the starting 51.2at.%Ni in the powder, LPBF samples are primary B2 with a tiny amount of B19'.

3.4. *B2↔B19' phase transformation*

Phase transformation was analysed via TEM observations over a range of temperatures to achieve a better understanding of the phases in the alloy. For this, the 55 J/mm^3 sample has been chosen, as it has a Ni Content of ~50.8at.%, a favourable composition in the use of stenting. A SEM image of the polished sample for taking the lamella and prior to

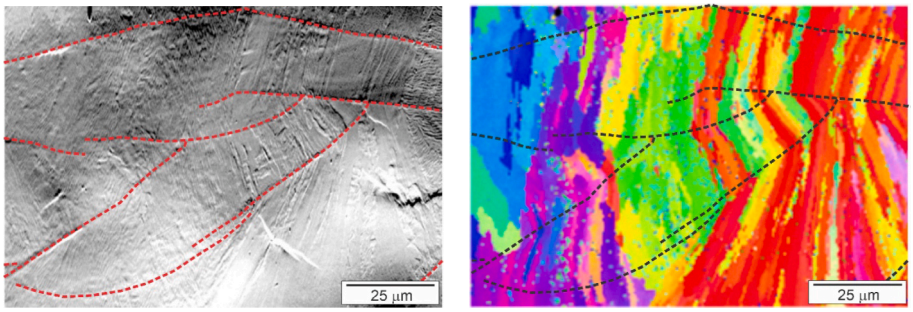

Fig. 6. Cross-sectional images (with build direction ↑) taken from the 55 J/mm^3 sample showing melt tracks and grains in (a) SEM micrograph and (b) EBSD texture orientation map.

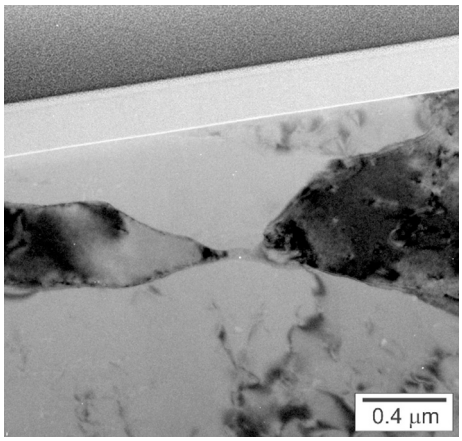

Fig. 7. Titan BF-TEM image taken at room temperature.

etching is presented in Fig. 6a, showing that the grains are not very clear but track boundaries can be traced. For reference, these boundaries have then been superimposed in the EBSD map in Fig. 6b. Grains are seen to grown either in the same direction or bend sharply crossing the track boundary. The grains within a track do not bend and are straight following the combination of the direction of heat flow and the grain growth preferred orientation during LPBF, as is commonly understood [1]. This grain feature is different to that of the alloy for stenting application using the traditional manufacturing route in which there are various forms of hot and then cold working and heat treating [42,43]. Thus, grain structures of traditional stents may be elongated grains with texture formed or equiaxed grains. Evident in Fig. 6b is the large variance in grain size, with grain widths from a few μm's to >10 μm. Thus, there could be several grains in the lamella of up to 10 μm wide and deep.

Examination and analysis via TEM began with an attempt to find martensite in the lamella at room temperature. A TEM image of the lamella is presented in Fig. 7. From a careful search of the entire lamella, no twinned martensite B19' was observed in the sample, suggesting that the sample entirely consists of the B2 austenite phase. However, the lamella sample is ~10 μm × 10 μm containing a few grains and as such the absence of B19' in this lamella does not mean an absence of B19' in the entire built sample, as corroborated by XRD which detected the presence of martensite.

The lamella was then examined for its phase transformation by cooling the sample below 0°. A TEM image at room temperature is presented in Fig. 8a, with a completely austenitic microstructure as comparably seen in Fig. 7. After decreasing and holding the temperature at −170 °C (Fig. 8b), the sample becomes fully martensitic, with an appearance similarly observed in the same alloy in a recent study [27]. From the minima of −170° the lamella was gradually heated up to

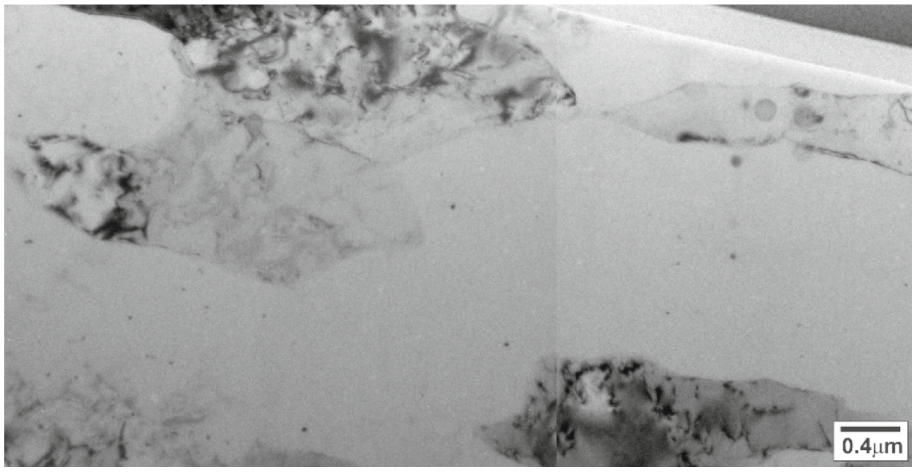

(a)

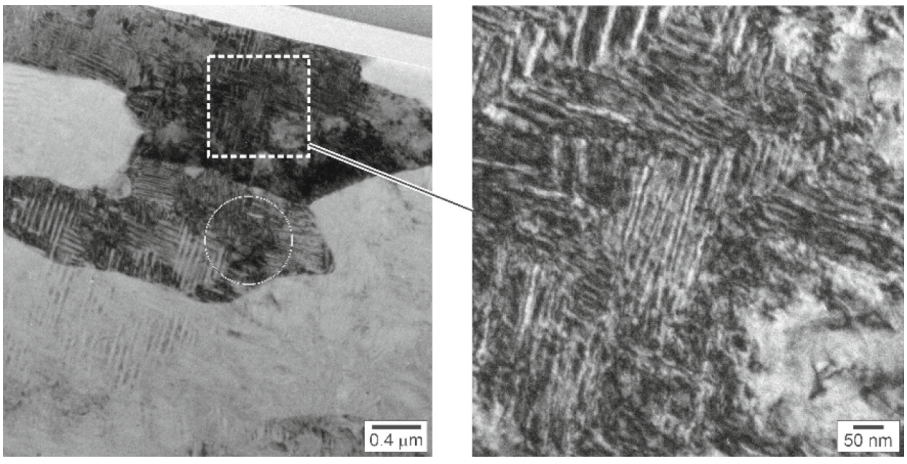

(b)

Fig. 8. Tecnai TEM images of the lamella (a) at room temperature, (b) after cooling and holding at −170 °C.

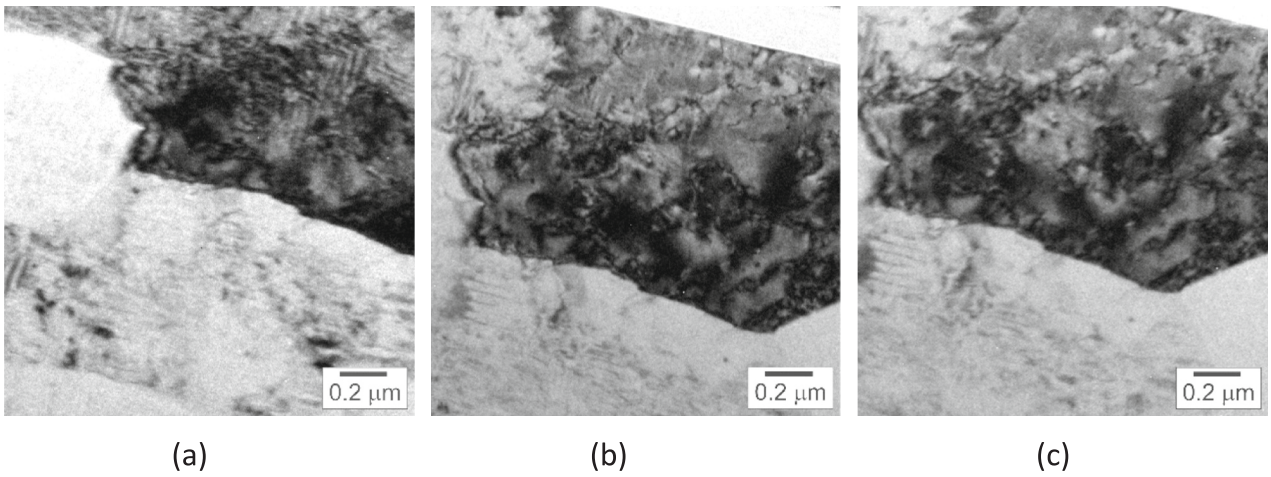

Fig. 9. Tecnai TEM images taken with the lamella temperature at (a) -80 °C displaying martensitic structure, (b) -64 °C displaying the dark grain having started transferring to austenite, and (c) -48 °C displaying the dark grain more transferred to austenite.

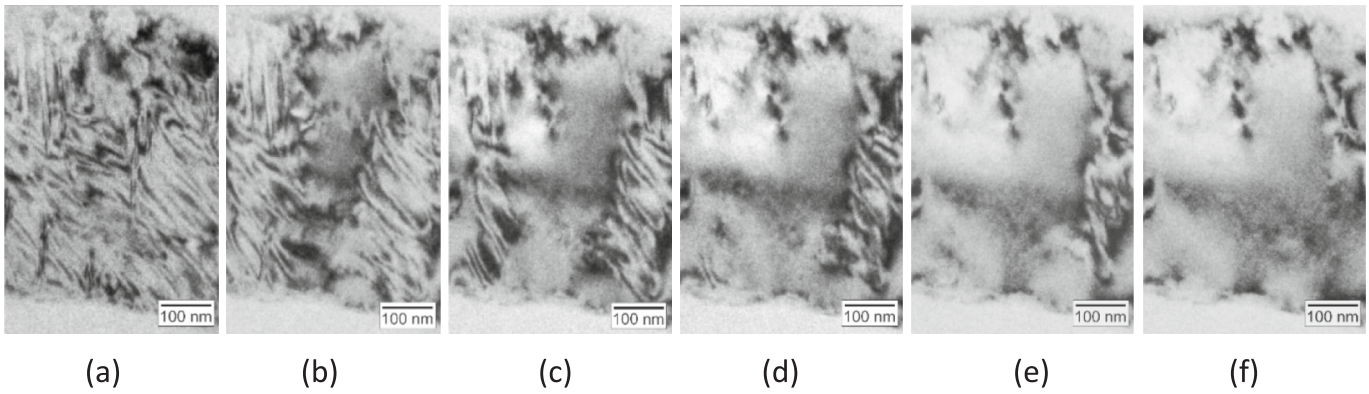

Fig. 10. Tecnai TEM images showing locally B19' to B2 transformation at temperatures of: (a) -19 °C, (b) -12 °C, (c) -10 °C, (d) -7 °C, (e) -3°, and (f) 0 °C.

−80 °C, whilst under observation. During this heating stage no M → A transformation was observed.

Temperature of the sample was then increased from −80 °C to −40 °C whilst being recorded under observation. An example of the M → A transformation can be observed in Fig. 9. At the onset (−80 °C), the dark grain on the top of Fig. 9a displays a martensitic grain morphology. The adjacent grain below also displays martensitic appearance although its brightness is high so the structure is less clear. At −64 °C, Fig. 9b, transformation began in the dark grain. In the later stage of this temperature increasing period, as shown in Fig. 9c, a large part of the darker grain is no longer martensitic and is instead largely austenitic. The grain below is however likely still fully martensitic. This suggests that after the nucleation of B2 in a grain, B19' → B2 may readily spread within that grain but not easily spread to next grain. It should be noted that the images in Fig. 9 are "screenshots" from the video. During the stage of increasing the sample temperature, the image gradually became defocused, with focus adjustments needed and made during the heating stage.

While B19' → B2 started at ~ − 64 °C, the transformation in other grains started at higher temperatures. The brighter grain in the lower part of Fig. 9 has illustrated that the transformation may not have started at the end of that heating period (40 °C). Fig. 10 illustrates the transformation in a grain that was still martensitic at −20° and almost completes the B19' → B2 transformation during the next increase in temperature to 0 °C. At −19 °C (Fig. 10a), B19' → B2 may have just started in the grain. When the temperature decreased to −12 °C, as shown in Fig. 10b, a significant portion in the mid-area of that locality in the image had transformed to B2. With an increase in temperature to −10 °C (Fig. 10c), B19' had transformed to B2 across the whole mid-area. As temperature continued to increase to −7 °C (Fig. 10d), −3 °C (Fig. 10e) and then to 0 °C, the whole portion of that grain in the images had become almost fully B2. A range of temperature over which B19' → B2 takes place directly observed here is consistent with the commonly indirectly observed transformation detected using differential scanning calorimetry (DSC) method, as has been well reviewed [5,10].

The observations of Fig. 10f suggest B19' → B2 transformation being almost complete at 0 °C may be seen to be inconsistent with the XRD result in Fig. 5 which notes at room temperature there is a tiny amount of B19'. However, XRD analysis over an area of few millimetres in width and in length, a few hundred thousand times larger than the area of a TEM lamella. The X-ray penetration and thus analytical depth is also a few hundred times larger than the thickness of a lamella. This difference in analytical volume must be taken into consideration. B19' → B2 takes place over a temperature range and this transformation is a gradual process meaning that the transformation takes place earlier in some grains and later in others. Observing the TEM sample in Fig. 9 the $A_s \approx -64$ °C and in Fig. 10 a $A_f \approx 0$ °C, in the small volume of TEM sample. Considering a volume of the same material more than a hundred-thousand times larger than the TEM lamella sample with B19' → B2 to occur, there could be locations where $A_f > 0$ °C. Thus, a tiny amount of B19' detected by XRD at room temperature would be viewed to be reasonable.

4. Conclusions

Using a pulse laser powder bed fusion (LPBF) machine for printing

Nitinol, defect free samples are achieved at laser energies (E) between 50 and 60 J/mm^3, with lack of fusion defect formation below and keyhole porosity above this E range. The rate of loss of Ni content with E is found to follow an exponential decay trend. Starting with the powder of Ni = 51.2at%, in the built sample using the minimum defect-level LPBF condition of 55 J/mm^3, Ni ≈ 50.8at% (the desirable Ni content). X-ray diffraction at room temperature shows that the structure is primarily austenite (B2) with a tiny amount of twinned martensite (B19') and that generally the amount of B19' increases with increasing E following the trend in increasing Ni loss with E. Sequential transmission electron micrographs of a lamella taken from the defect-free and Ni ≈ 50.8at% sample have shown that B19' → B2 took place over the temperature range of −64- 0 °C. The B19' → B2 transformation likely occurs grain-by-grain, with B19' → B2 transformation starting in one grain within that temperature range and completing solely in that grain as temperature increases.

CRediT authorship contribution statement

Erika Maria Sequeda Leon: Writing – original draft, Methodology, Investigation, Formal analysis, Data curation. **Teresa Guraya:** Writing – review & editing, Writing – original draft, Supervision, Resources, Methodology, Investigation, Formal analysis, Data curation. **Xabier Lasheras:** Methodology, Formal analysis. **Ana Okariz:** Methodology, Formal analysis, Data curation. **Karl Peter Davidson:** Writing – review & editing. **Sarat Singamneni:** Supervision, Resources, Methodology. **Zhan Wen Chen:** Writing – review & editing, Writing – original draft, Supervision, Methodology, Investigation, Formal analysis, Data curation, Conceptualization.

Declaration of competing interest

We have no conflicts of interest to declare.

Acknowledgments

Authors acknowledge the use of instrumentation as well as the technical advice provided by the National Facility ELECMI ICTS, node «Laboratorio de Microscopias Avanzadas (LMA)» at «Universidad de Zaragoza» and by Azterlan-BRTA.

Data availability

The raw/processed data required to reproduce these findings cannot be shared.

References

[1] T. DebRoy, H.L. Wei, J.S. Zuback, T. Mukherjee, J.W. Elmer, J.O. Milewski, A. M. Beese, A. Wilson-Hid, A. De, W. Zhang, Additive manufacturing of metallic components - process, structure and properties, Prog. Mater. Sci. 92 (2018) 112–224.
[2] I.M. Kusoglu, B. Gökce, S. Barcikowski, Research trends in laser powder bed fusion of Al alloys within the last decade, Addit. Manuf. 36 (2020) 101489.
[3] Z. Wu, S.P. Narra, A. Rollett, Exploring the fabrication limits of thin-wall structures in a laser powder bed fusion process, Int. J. Adv. Manuf. Technol. 110 (2020) 191–207.
[4] H.Y. Ma, J.C. Wang, P. Qin, Y.J. Liu, L.Y. Chen, L.Q. Wang, L.C. Zhang, Advances in additively manufactured titanium alloys by powder bed fusion and directed energy deposition: microstructure, defects, and mechanical behavior, J. Mater. Sci. Technol. 183 (2024) 32–62.
[5] M. Elahinia, N.S. Moghaddam, M.T. Andani, A. Amerinatanzi, B.A. Bimber, R. F. Hamilton, Fabrication of NiTi through additive manufacturing: a review, Prog. Mater. Sci. 83 (2016) 630–663.
[6] W.S.W. Harun, M.S.I.N. Kamariah, N. Muhamad, S.A.C. Ghani, F. Ahmad, Z. Mohamed, A review of powder additive manufacturing processes for metallic biomaterials, Powder Technol. 327 (2018) 128–151.
[7] K. Safaei, H. Abedi, M. Nematollahi, F. Kordizadeh, H. Dabbaghi, P. Bayati, R. Javanbakht, A. Jahadakbar, M. Elahinia, B. Poorganj, Additive manufacturing of NiTi shape memory alloy for biomedical applications: review of the LPBF process ecosystem, JOM 73 (2021) 3771–3786.
[8] A.N. Alagh, S. Hussain, W. Zaki, Additive manufacturing of shape memory alloys: a review with emphasis on powder bed systems, Mater. Des. 204 (2021) 109654.
[9] O.A. Mohamed, S.H. Masood, W. Xu, Nickel-titanium shape memory alloys made by selective laser melting: a review on process optimisation, Addit. Manuf. 19 (2022) 24–58.
[10] M. Sathishkumar, C.P. Kumar, S.S.S. Ganesh, M. Venkatesh, N. Radhika, M. Vignesh, P. Ashwath, Possibilities, performance and challenges of nitinol alloy fabricated by directed energy deposition and powder bed fusion for biomedical implants, J. Manuf. Process. 102 (2023) 885–909.
[11] S. Wei, J. Zhang, L. Zhang, Y. Zhang, B. Song, X. Wang, J. Fan, Q. Liu, Y. Shi, Laser powder bed fusion additive manufacturing of NiTi shape memory alloys: a review, Int. J. Extrem. Manufactur. 5 (2023) 032001.
[12] M. Jalali, K. Mohammadi, M.R. Movahhedy, F. Karimi, S.K. Sadrnezhaad, S. V. Chernyshikhin, V. Igor, S.L.M. Shishkovsky, Additive Manufacturing of NiTi Porous Implants: A Review of Constitutive Models, Finite Element Simulations, Manufacturing, Heat Treatment, Mechanical, and Biomedical Studies, Met. Mater. Int. 29 (2023) 2458–2491.
[13] T.C. Dzogbewu, D.J. de Beer, Additive manufacturing of NiTi shape memory alloy and its industrial applications, Heliyon 10 (2024) e23369.
[14] T.W. Duerig, D.E. Tolomeo, M. Wholey, An overview of superelastic stent design, Minim. Invasive Ther. Allied Technol. 9 (2000) 235–246.
[15] D. Stoeckel, Nitinol medical devices and implants, Minim. Invasive Ther. Allied Technol. 9 (2) (2000) 81–88.
[16] A.R. Pelton, J. DiCello, S. Miyazaki, Optimisation of processing and properties of medical grade nitinol wire, Minim. Invasive Ther. Allied Technol. 9 (1) (2000), 107–1 18.
[17] S.W. Robertson, A. Mehta, A.R. Pelton, R.O. Ritchie, Evolution of crack-tip transformation zones in superelastic nitinol subjected to in situ fatigue: a fracture mechanics and synchrotron X-ray microdiffraction analysis, Acta Mater. 55 (2007) 6198–6207.
[18] A.R. Pelton, V. Schroeder, M.R. Mitchell, M. XiaoYan Gong, S.W. Robertson Barney, Fatigue and durability of nitinol stents, J. Mech. Behav. Biomed. Mater. 1 (2008) 153–164.
[19] E. Henderson, D.H. Nash, W.M. Dempster, On the experimental testing of fine nitinol wires for medical devices, J. Mech. Behav. Biomed. Mater. 4 (2011) 261–268.
[20] J. Frenzel, E.P. George, A. Dlouhy, C. Somsen, M. Wagner, G. Eggeler, Influence of Ni on martensitic phase transformations in NiTi shape memory alloys, Acta Mater. 58 (2010) 3444–3458.
[21] N.S. Moghaddam, S. Saedi, A. Amerinatanzi, A. Hinojos, A. Ramazani, J. Kundin, M.J. Mills, H. Karaca, M. Elahinia, Achieving superelasticity in additively manufactured NiTi in compression without post-process heat treatment, Sci. Rep. 9 (2019) 41.
[22] L. Xue, K.C. Atli, S. Picak, C. Zhang, B. Zhang, A. Elwany, R. Arroyave, I. Karaman, Controlling martensitic transformation characteristics in defect-free NiTi shape memory alloys fabricated using laser powder bed fusion and a process optimization framework, Acta Mater. 215 (2021) 117017.
[23] S.E. Saghaian, M. Nematollahi, G. Toker, A. Hinojos, N.S. Moghaddam, S. Saedi, C. Y. Lu, M.J. Mahtabi, M.J. Mills, M. Elahinia, H.E. Karaca, Effect of hatch spacing and laser power on microstructure, texture, and thermomechanical properties of laser powder bed fusion (L-PBF) additively manufactured NiTi, Opt. Laser Technol. 149 (2022) 107680.
[24] G. Carlucci, L. Patriarca, A.G. Demir, J.N. Lemke, A. Coda, B. Previtali, R. Casati, Building orientation and heat treatments effect on the Pseudoelastic properties of NiTi produced by LPBF, Shap. Mem. Superelasticit. 8 (2022) 235–247.
[25] K. Khanlari, Q. Shi, X. Yan, K. Hu, C. Tan, P. Kelly, W. Zhang, P. Cao, X. Wang, X. Liu, Printing of NiTinol parts with characteristics respecting the general microstructural, compositional and mechanical requirements of bone replacement implants, Mate. Sc. & Eng. A 839 (2022) 142839.
[26] Hao Jiang, Xiebin Wang, Rui Xi, Guichuan Li, Huiliang Wei, Jiangwei Liu, Bo Zhang, Sergey Kustov, Kim Vanmeensel, Jan Van Humbeeck, Guoqun Zhao, Size effect on the microstructure, phase transformation behavior, and mechanical properties of NiTi shape memory alloys fabricated by laser powder b e d fusion, J. Mater. Sci. Technol. 157 (2023) 200–212.
[27] N. Zeleznik, A. Hinojos, X. Gao, M. Nematollahi, N.S. Moghaddam, S. Saedi, W. Zhang, M. Elahinia, H. Karaca, J. McGuffin-Cawley, M. Mills, P.M. Anderson, Modeling the Pseudoelastic design space of NiTi fabricated by laser powder bed fusion, Addit. Manuf. 66 (2023) 103472.
[28] J. Chen, Z. Liu, C. Liu, B. Zhang, T. Liu, G. Chen, M. Qin, X. Qu, Effects of scanning strategy and scanning speed on microstructures and mechanical properties of NiTi alloys by laser powder bed fusion, Mate. Sc. & Eng. A 914 (2024) 147115.
[29] M.A. Obeidi, M. Monu, C. Hughes, D. Bourke, M.N. Dogu, J. Francis, M. Zhang, I. U. Ahad, D. Brabazon, Laser beam powder bed fusion of nitinol shape memory alloy (SMA), J. Mater. Res. Technol. 14 (2021) 2554–2570.
[30] W. Chen, Q. Yang, S. Huang, S. Huang, J.J. Kruzic, X. Li, Laser power modulated microstructure evolution, phase transformation and mechanical properties in NiTi fabricated by laser powder bed fusion, J. Alloys Compd. 861 (2021) 157959.
[31] A. Safdel, M.A. Elbestawi, New insights on the laser powder bed fusion processing of a NiTi alloy and the role of dynamic restoration mechanisms, J. Alloys Compd. 885 (2021) 160971.
[32] S. Maffia, V. Finazzi, F. Berti, F. Migliavacca, L. Petrini, B. Previtali, A.G. Demir, Selective laser melting of NiTi stents with open-cell and variable diameter, Smart Mater. Struct. 30 (2021) 105010.
[33] J. Zhu, E. Borisov, X. Liang, E. Farber, M.J.M. Hermans, V.A. Popovich, Predictive analytical modelling and experimental validation of processing maps in additive manufacturing of nitinol alloys, Addit. Manuf. 38 (2021) 101802.

[34] M.A. Obeidi, Achieving high quality nitinol parts with minimised input thermal energy by optimised pulse wave laser powder bed fusion process, Result. Mater. 14 (2022) 100279.
[35] W. Guo, B. Feng, Y. Yang, Y. Ren, Y. Liu, H. Yang, Q. Yang, L. Cui, X. Tong, S. Hao, Effect of laser scanning speed on the microstructure, phase transformation and mechanical property of NiTi alloys fabricated by LPBF, Mater. Des. 215 (2022) 110460.
[36] F.L. Shen, H.Q. Li, H. Guo, N.N. Guo, X.Y. Fang, Effect of energy density on the superelastic property of Ni-rich NiTi alloy fabricated by laser powder bed fusion, Mater. Sci. Eng. A 854 (2022) 143874.
[37] J. Zhan, J. Wu, R. Ma, K. Li, T. Huang, J. Lin, L.E. Murr, Effect of microstructure on the superelasticity of high-relative-density Ni-rich NiTi alloys fabricated by laser powder bed fusion, J. Mater. Processi. Tech. 317 (2023) 117988.
[38] J. Zhan, J. Wu, R. Ma, K. Li, J. Lin, L.E. Murr, Tuning the functional properties by laser powder bed fusion with partitioned repetitive laser scanning: toward editable 4D printing of NiTi alloys, J. Manuf. Process. 101 (2023) 1468–1481.
[39] J. Wang, R. Zhu, Y. Liu, L. Zhang, Understanding melt pool characteristics in laser powder bed fusion: an overview of single- and multi-track melt pools for process optimization, Adv. Powder Mater. 2 (2023) 100137.
[40] Joint Committee on Powder Diffraction Standards (JCPDS), Powder Diffraction File-Inorganic, International Centre for Diffraction Data, Swarthmore, NJ, 1997.
[41] M. Rui Miguel Dos Santos, In-Situ x-Ray Diffraction Studies during Growth of Ni-Ti Shape Memory Alloy Films and their Complementary Ex-Situ Characterization, PhD thesis,, New University of Lisbon, 2008, p. p224.
[42] M.M. Barney, D. Xu, S.W. Robertson, V. Schroeder, R.O. Ritchie, A.R. Pelton, A. Mehta, Impact of thermomechanical texture on the superelastic response of nitinol implants, J. Mech. Behav. Biomed. Mater. (2011) 1431–1439.
[43] E. Twohig, P. Tiernan, J. Butler, C. Dickinson, S.A.M. Tofail, Mechanical, microstructural and thermal properties of a 50:50 at.% nickel–titanium alloy subjected to a dieless drawing process, Acta Mater. 68 (2014) 140–149.